Shock wave propagation along the central retinal blood vessels: Supplementary material

T. A. Spelman* & P. S. Stewart*

February 5, 2020

In this supplementary material we expand on several sections of the main paper. In particular, we expand the model derivation and description of the numerical schemes (Sec. S1), provide some supplementary numerical results to expand those given in the main text (Sec. S2), provide some additional analytical results (Sec. S3) and also consider the energetics of the motion (Sec. S4).

S1 The model

In this section we derive the long-wavelength model used in each region from the Navier–Stokes equations (Sec. S1.1) and provide more details of the two numerical schemes that we employ (Sec. S1.2).

S1.1 Derivation of the long-wavelength model

We consider a long blood vessel of length L^* and baseline cross-sectional area A_0^*. This vessel is described using cylindrical polar coordinates (r^*, θ, x^*), where r^* and θ represent the radial and azimuthal coordinates, respectively, and x^* is measured along the axis of the tube with corresponding unit vectors $\mathbf{e}_r$, $\mathbf{e}_\theta$ and $\mathbf{e}_x$. Time is denoted t^*.

The flow of blood is assumed to be homogeneous and Newtonian, appropriate for blood vessels of diameter greater than $100\mu m$ [3]. We denote the (constant) viscosity and density of the blood as μ^* and ρ^*, respectively.

The elastic portions of the wall are assumed to exhibit an elastic pre-stress Γ^* and an elastic stiffness k^*. In general the vessel wall is assumed to be located at a radius $r^* = R^*(\theta, x^*, t^*)$ and the vessel cross-sectional area is denoted $A^*(x^*, t^*)$. The corresponding volume of the vessel (used for checking conservation of mass in Sec. S1.2 below) is then defined as

$$V^*(x^*, t^*) = \int_{L^*} A^*(x^*, t^*)\ \mathrm{d}x^*. \tag{S1}$$

Furthermore, the baseline pressure external to the vessel is denoted p_0^*.

*School of Mathematics and Statistics, The Mathematics and Statistics Building, University Place, University of Glasgow, Glasgow, UK. G12 8SQ

We non-dimensionalise all lengths on the square root of the baseline cross-sectional area $A_0^{*1/2}$, velocities on $U_0^* = (k^*/\rho^*)^{1/2}$, time on $t_0^* = (\rho^* A_0^*/k^*)^{1/2}$ and pressures according to

$$p^* = k^* p + p_0^*. \tag{S2}$$

All dimensionless variables are denoted with the same symbol as their dimensional counterpart without the asterisk. This choice of non-dimensional scales results in the following dimensionless groups

$$L = \frac{L^*}{A_0^{*1/2}}, \qquad \mathcal{R} = \frac{\rho^* U_0^* A_0^{*1/2}}{\mu^*}, \qquad \Gamma = \frac{\Gamma^*}{k^* A_0^{*1/2}}. \tag{S3}$$

There are additional dimensionless parameters associated with the geometry of each individual region and the pressure perturbation, which are defined in the main text.

Hence, the dimensionless flow velocity $\mathbf{u} = u_r\mathbf{e}_r + u_\theta\mathbf{e}_\theta + u_x\mathbf{e}_x$ and dimensionless blood pressure p follow the non-dimensional Navier–Stokes equations

$$\nabla \cdot \mathbf{u} = 0, \qquad \frac{\partial \mathbf{u}}{\partial t} + \mathbf{u} \cdot \nabla \mathbf{u} = -\nabla p + \mathcal{R}^{-1}\nabla^2 \mathbf{u}, \tag{S4}$$

where the gradient operator is defined in (dimensionless) cylindrical polar coordinates. We apply kinematic boundary conditions on the tube wall in the form

$$u_r = \frac{\partial R}{\partial t} + \frac{u_\theta}{R}\frac{\partial R}{\partial \theta} + u_x \frac{\partial R}{\partial x}, \qquad (r = R), \tag{S5}$$

along with a normal stress balance (Eq. (S6) discussed below). Further boundary conditions are required if the flow is viscous.

We henceforth assume that the flow is axis-symmetric, so all variables are independent of the polar coordinate θ and the azimuthal component of the fluid velocity is zero ($u_\theta = 0$).

We consider an elastic response to displacement of the wall in the form of a tube law with axial tension,

$$p = p_b + \mathcal{F}(A) - \Gamma A_{xx}, \qquad (r = R), \tag{S6}$$

where $\mathcal{F}$ is a nonlinear function of the local tube radius (a 'tube law') representing the local resistance to expansion or compression. A similar tube law including axial tension was considered by [2] and related papers.

Since the blood vessels are typically long compared to their radius, we reduce the complexity of the system using a long-wavelength approximation. In particular, we construct a small parameter $\beta = 1/L \ll 1$ and rescale the variables according to

$$r = \tilde{r}, \quad x = \beta^{-1}\tilde{x}, \quad t = \beta^{-1}\tilde{t}, \quad u_r = \beta\tilde{u}_r, \quad u_x = \tilde{u}_x, \quad p = \tilde{p}, \quad R = \tilde{R}, \quad A = \tilde{A}, \tag{S7}$$

and the model parameters according to

$$\tilde{\Gamma} = \beta^2\Gamma = \frac{\Gamma^* A_0^{*1/2}}{L^{*2} k^*}, \qquad \tilde{\mathcal{R}} = \beta\mathcal{R} = \frac{\rho^* A_0^* U_0^*}{\mu^* L^*}. \tag{S8}$$

Note that all long wavelength variables and parameters are denoted with a tilde.

The final system of governing equations, neglecting terms of $O(\beta^2)$, can be written as

$$\frac{1}{\tilde{r}}\frac{\partial}{\partial\tilde{r}}(\tilde{r}\tilde{u}_r)+\frac{\partial\tilde{u}_x}{\partial\tilde{x}}=0, \tag{S9}$$

$$\frac{\partial\tilde{p}}{\partial\tilde{r}}=0, \tag{S10}$$

$$\frac{\partial\tilde{u}_x}{\partial\tilde{t}}+\tilde{u}_r\frac{\partial\tilde{u}_x}{\partial\tilde{r}}+\tilde{u}_x\frac{\partial\tilde{u}_x}{\partial\tilde{x}}=-\frac{\partial\tilde{p}}{\partial\tilde{x}}-\frac{1}{\tilde{\mathcal{R}}}\frac{1}{\tilde{r}}\frac{\partial}{\partial\tilde{r}}\left(\tilde{r}\frac{\partial\tilde{u}_r}{\partial\tilde{r}}\right). \tag{S11}$$

subject to a (dimensionless) long wavelength kinematic condition

$$\tilde{u}_r=\frac{\partial\tilde{R}}{\partial\tilde{t}}+\tilde{u}_x\frac{\partial\tilde{R}}{\partial\tilde{x}},\qquad(\tilde{r}=\tilde{R}). \tag{S12}$$

Following Stewart *et al.* (2009) [4], we integrate the governing equations (S9) and (S11) across the vessel cross-section to reduce the system to PDEs in one spatial dimension. The conservation of mass equation (S9) becomes

$$2\pi\left[\tilde{r}\tilde{u}_r\right]_0^{\tilde{R}}+2\pi\int_0^{\tilde{R}}\frac{\partial\tilde{u}_x}{\partial\tilde{x}}\,\tilde{r}\mathrm{d}\tilde{r}=0. \tag{S13}$$

The first term can be evaluated directly and the integral in the second term can be manipulated to write the system in the form

$$2\pi\tilde{R}\tilde{u}_r(\tilde{r}=\tilde{R})+2\pi\frac{\partial}{\partial\tilde{x}}\int_0^{\tilde{R}}\tilde{u}_x\,\tilde{r}\mathrm{d}\tilde{r}-\pi\tilde{R}\frac{\partial\tilde{R}}{\partial x}\tilde{u}_x|_{\tilde{r}=\tilde{R}}=0. \tag{S14}$$

Substituting the kinematic condition (S12) on the interface we obtain

$$2\pi\tilde{R}\frac{\partial\tilde{R}}{\partial\tilde{t}}+2\pi\frac{\partial}{\partial\tilde{x}}\int_0^{\tilde{R}}\tilde{u}_x\,\tilde{r}\mathrm{d}\tilde{r}=0. \tag{S15}$$

Since the tube is assumed axis-symmetric we express the first term entirely in terms of $\tilde{A}=\pi\tilde{R}^2$, in the form

$$\frac{\partial\tilde{A}}{\partial\tilde{t}}+2\pi\frac{\partial}{\partial\tilde{x}}\int_0^{\tilde{R}}\tilde{u}_x\,\tilde{r}\mathrm{d}\tilde{r}=0. \tag{S16}$$

The axial flux along the vessel takes the form

$$\tilde{q}=2\pi\int_0^{\tilde{R}}\tilde{u}_x\,\tilde{r}\mathrm{d}\tilde{r}, \tag{S17}$$

and so (S9) reduces to the familiar form

$$\frac{\partial\tilde{A}}{\partial\tilde{t}}+\frac{\partial\tilde{q}}{\partial\tilde{x}}=0. \tag{S18}$$

Similarly, the conservation of momentum equation (S11) becomes

$$2\pi\int_0^{\tilde{R}}\frac{\partial\tilde{u}_x}{\partial\tilde{t}}\tilde{r}\mathrm{d}\tilde{r}+\int_0^{\tilde{R}}\left(\tilde{u}_r\frac{\partial\tilde{u}_x}{\partial\tilde{r}}+\tilde{u}_x\frac{\partial\tilde{u}_x}{\partial\tilde{x}}\right)\tilde{r}\mathrm{d}\tilde{r}=-2\pi\int_0^{\tilde{R}}\frac{\partial\tilde{p}}{\partial\tilde{x}}\,\tilde{r}\mathrm{d}\tilde{r}-\frac{2\pi}{\tilde{\mathcal{R}}}\left[\tilde{r}\frac{\partial\tilde{u}_r}{\partial\tilde{r}}\right]_0^{\tilde{R}}. \tag{S19}$$

Manipulating the convective inertia terms using the conservation of mass equation, and again cancelling boundary terms using the kinematic condition (S12), we derive

$$2\pi\frac{\partial}{\partial\tilde{t}}\int_0^{\tilde{R}}\tilde{u}_x\,\tilde{r}\mathrm{d}\tilde{r}+2\pi\frac{\partial}{\partial\tilde{x}}\left(\int_0^{\tilde{R}}\tilde{u}_x^2\,\tilde{r}\mathrm{d}\tilde{r}\right)=-2\pi\int_0^{\tilde{R}}\frac{\partial\tilde{p}}{\partial\tilde{r}}\,\tilde{r}\mathrm{d}\tilde{r}+\frac{2\pi}{\tilde{\mathcal{R}}}\tilde{R}\,\frac{\partial\tilde{u}_r}{\partial\tilde{r}}\bigg|_{\tilde{r}=\tilde{R}}. \tag{S20}$$

We can easily rewrite the unsteady inertia in terms of the axial flux, and manipulate the pressure gradient term using (S10) so that the axial momentum equation becomes

$$\frac{\partial\tilde{q}}{\partial\tilde{t}}+2\pi\frac{\partial}{\partial\tilde{x}}\left(\int_0^{\tilde{R}}\tilde{u}_x^2\,\tilde{r}\mathrm{d}\tilde{r}\right)=-2\pi\int_0^{\tilde{R}}\frac{\partial\tilde{p}}{\partial\tilde{r}}\,\tilde{r}\mathrm{d}\tilde{r}+\frac{2\pi}{\tilde{\mathcal{R}}}\tilde{R}\,\frac{\partial\tilde{u}_r}{\partial\tilde{r}}\bigg|_{\tilde{r}=\tilde{R}}. \tag{S21}$$

Noting that p is independent of r through (S10), we can integrate the first term on the RHS to obtain

$$\frac{\partial\tilde{q}}{\partial\tilde{t}}+2\pi\frac{\partial}{\partial\tilde{x}}\left(\int_0^{\tilde{R}}\tilde{u}_x^2\,\tilde{r}\mathrm{d}\tilde{r}\right)=-A\frac{\partial\tilde{p}}{\partial\tilde{x}}+\frac{2\pi}{\tilde{\mathcal{R}}}\tilde{R}\,\frac{\partial\tilde{u}_r}{\partial\tilde{r}}\bigg|_{\tilde{r}=\tilde{R}}. \tag{S22}$$

In the main text we close this system by assuming the blood is approximately inviscid over the timescales considered, so we approximate $\tilde{u}_x=\tilde{u}_x(\tilde{x},\tilde{t})$ (a plug flow independent of $\tilde{r}$) and take the limit $\tilde{\mathcal{R}}\to\infty$. This assumption means that the axial flux reduces to the simple form $\tilde{q}=\tilde{A}\tilde{u}_x$ and the governing equations can be reduced to two coupled PDEs in $\tilde{A}$ and $\tilde{q}$ alone,

$$\frac{\partial\tilde{A}}{\partial\tilde{t}}+\frac{\partial\tilde{q}}{\partial\tilde{x}}=0,\qquad\frac{\partial\tilde{q}}{\partial\tilde{t}}+\frac{\partial}{\partial\tilde{x}}\left(\frac{\tilde{q}^2}{\tilde{A}}\right)=-\tilde{A}\frac{\partial\tilde{p}}{\partial\tilde{x}}, \tag{S23}$$

given in (2.5) in the main text.

In the limit of zero membrane tension this system is identical to that derived by [3] and the governing equations can be combined into a single equation in conservation form

$$\left(\frac{\partial}{\partial\tilde{t}}+(\tilde{u}_x\pm\tilde{c})\frac{\partial}{\partial\tilde{x}}\right)\left[\tilde{u}_x\pm\int_1^{\tilde{A}}\frac{\tilde{c}}{\tilde{A}'}\,d\tilde{A}'\right]=0,\qquad\tilde{c}^2=\tilde{A}\frac{\mathrm{d}\mathcal{F}}{\mathrm{d}\tilde{A}}, \tag{S24}$$

where $\tilde{c}$ is the nonlinear wavespeed and the Riemann invariants take the form

$$\tilde{u}_x\pm\int_1^{\tilde{A}}\frac{\tilde{c}}{\tilde{A}'}\,d\tilde{A}'. \tag{S25}$$

This system is hyperbolic, and we can estimate the local Mach number of the flow as

$$M(x,t)=\frac{\tilde{u}_x(x,t)}{\tilde{c}(x,t)}. \tag{S26}$$

To estimate a global Mach number for the entire system we compute $\overline{M}=\max_t(\max_x(M))$.

However, if the fluid is assumed to be viscous this long-wavelength system of equations (S9-S11) is not closed. In the literature on flow in collapsible tubes a number of approaches are used to close the system based on specific assumptions or empirical measurements [2]. Below we consider a modified Hagen–Poiseuille flow profile in the form

$$\tilde{u}_x=\frac{4\tilde{q}}{\tilde{R}^4}(\tilde{R}^2-\tilde{r}^2),\qquad\qquad(0\le\tilde{r}\le\tilde{R}), \tag{S27}$$

which automatically applies the no-slip condition on the tube wall and results in an additional viscous term on the right hand side of (S23) in the form

$$\left.\frac{2\pi}{\tilde{\mathcal{R}}}\tilde{R}\,\frac{\partial \tilde{u}_r}{\partial \tilde{r}}\right|_{\tilde{r}} = S\frac{\tilde{q}}{\tilde{A}}, \qquad \text{where} \qquad S = \frac{8\pi}{\tilde{\mathcal{R}}}. \tag{S28}$$

Strictly speaking, this Poiseuille flow approximation also modifies the coefficient of the convective inertia term (becoming 4/3 rather than 1) but we ignore this extra inertial contribution in the viscous simulations in Sec. S2.2 below.

Applying this Hagen–Poiseuille flow model along a section of vessel of length 1mm results in a viscous pressure drop of $\approx$ 6mmHg for the CRA and $\approx$ 1.76 mmHg for the CRV. These are substantially smaller than the applied external pressures considered for arteries and veins in Fig. 4 of the main paper.

For the remainder of this supplementary information we drop tildes for notational convenience.

S1.2 Further details of the numerical schemes

Numerical simulations of both models were carried out on a variety of machines using MATLAB 2018b.

S1.2.1 Upwind Godunov scheme

As discussed in the main text, our shock capturing numerical scheme is based on the upwind Godunov finite volume scheme constructed by Brook *et al.* (1999) [1], which employs a Riemann solver at each point along the domain. We do not reproduce the details of that scheme here, but instead focus on the unique aspects of our scheme. In particular, to allow disturbances to pass between regions (which typically have discontinuous material properties) we do not use the Riemann solver at the region boundaries but instead separately determine the fluid flux and cross-sectional area on both sides of the junction (four unknowns) using a characteristic projection method. Along a given characteristic (in a given direction) the corresponding Riemann invariant in Eq. (S25) fixes the relationship between the fluid velocity u_x and the tube cross-sectional area A. As we approach the edge of the region (from either side) we numerically construct the characteristic by projecting from the interior grid point adjacent to the junction using a first-order upwind scheme [5]. This Riemann invariant provides an extra relationship between the variables at the junction. Hence, at the far upstream and downstream boundaries of the system we couple this Riemann invariant to the specified boundary condition which provides enough information to fix all dependent variables at the boundary. Similarly, at an interior boundary we use information from the two Riemann invariants (one coming from each direction) and the two given boundary conditions (continuity of fluid flux and continuity of pressure) to specify the dependent variables at the boundary.

For this method we typically used a spatial mesh size of $n = 300$ equally spaced intervals in each region with a Courant number of 0.05. Time-steps are chosen according to the maximum wavespeed at the previous timestep [1].

S1.2.2 Semi-implicit finite difference scheme

For the model which includes membrane tension, we used a semi-implicit finite difference numerical scheme which is fourth order in space and first order in time, as used previously for a similar

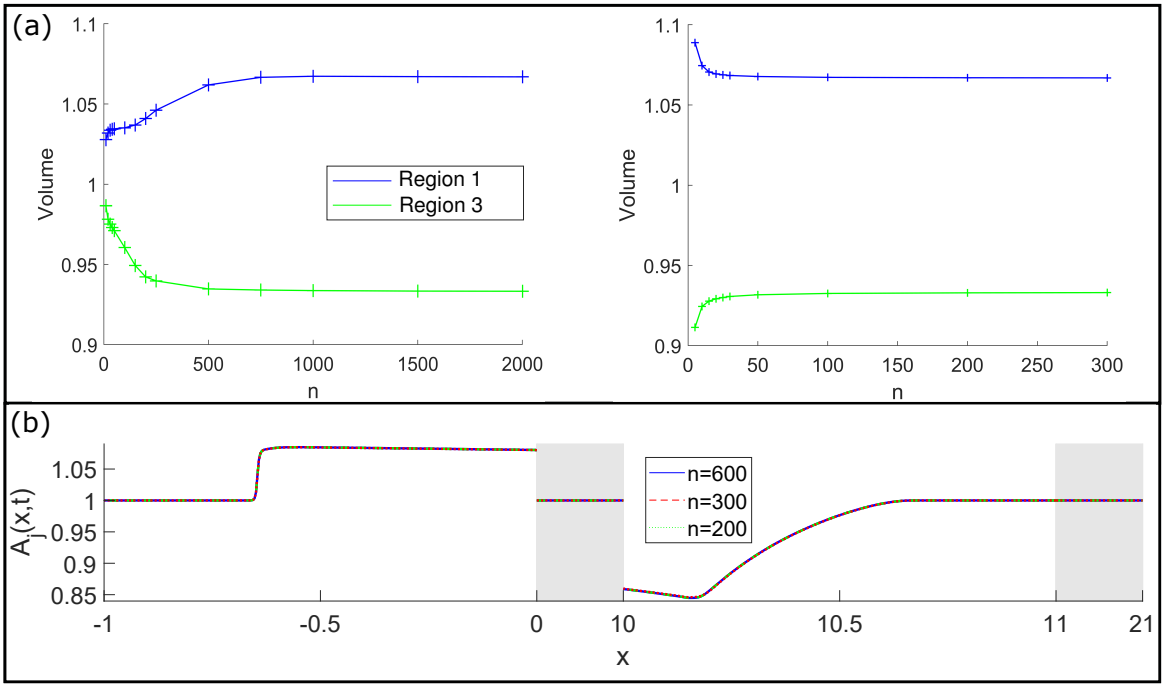

Figure S1: Convergence for the baseline case of $\Delta p = 75$ applied over $t_{ap} = 0.1$: (a) the region volume evaluated at $t = 0.24$ as a function of the number of spatial grid points, n, where the blue (green) curve is the volume of region 1 (region 3) for both the semi-implicit method with $\Gamma = 10^{-4}$ (left) and the shock capture upwind scheme (right); (b) the spatial profile of the tube cross-sectional area in regions 1 and 3 predicted by the shock-capture code evaluated at $t = 0.2$ for three different choices of n ($n = 600$: blue solid line, $n = 300$: red dashed line, $n = 200$: green dotted line.

system [4]. In particular, only the highest derivative term in each equation is treated implicitly, with the remaining terms treated explicitly. In simulation we typically used a spatial mesh size of $n = 2000$ equally spaced intervals in each region (as we must resolve the short wavelength dispersive waves around the sharp front) with a fixed non-dimensional time step of on the order of 10^{-4} to 10^{-5}. Again we verified convergence of our simulations by comparing to the predictions of both finer and coarser numerical grids (see Fig. S1).

S1.2.3 Verifying conservation of mass

As well as comparing the predictions of our two numerical models to each other and the analytical models, we also validated our predictions using finer spatial and temporal grids. For example, a convergence test is shown in Fig. S1 for the baseline case considering the retinal vein with $\Delta p = 75$ applied over $t_{ap} = 0.1$, for both the membrane tension model with a timestep of 1.2×10^{-4} (Fig. S1a, left hand panel) and the shock capture model using a Courant number of 0.05 (Fig. S1a, right hand panel). In particular we compute the volume of the two deforming regions at a fixed time after the pressure perturbation has been fully applied, as a function of the number of spatial grid intervals, denoted n. In both cases we observe large variations in region volume for small n (large spatial steps), but these differences become minimal as the mesh size approaches that used in our

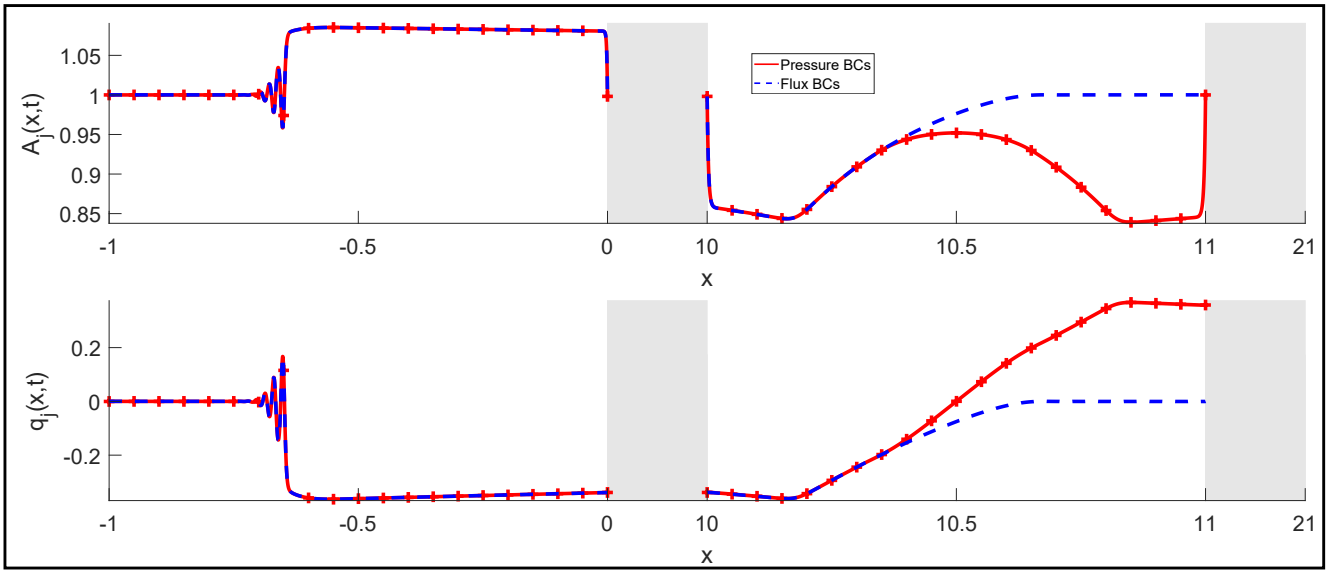

Figure S2: A typical snapshot of the spatial profiles of the vessel cross-sectional area (top) and axial flux (bottom) using fixed pressure boundary conditions at the end of the vessels (red) compared to the no flux boundary conditions (blue dashed line) in response to a pressure forcing of amplitude $\Delta p = 75$ applied over $t_{ap} = 0.1$.

simulations.

In addition, it is important to verify that the characteristic methods used between regions in our Godunov scheme are not unduly influencing the solution. In particular in Fig. S1(b) we consider a pressure perturbation $\Delta p = 75$ applied over $t_{ap} = 0.1$ using three different spatial resolutions with fixed Courant number (=0.05). Plotting the spatial profiles of the system a fixed time after initiation we find that the profiles with each of the three resolutions overlay perfectly, suggesting that our profiles are well converged.

S2 Additional Numerical Results

In this section we explore several other features of the shock propagation which we did not have space to discuss in the main text. In particular we explore the influence of prescribed downstream pressure boundary conditions (Sec. S2.1), the role of blood viscosity (Sec. S2.2), the role of the membrane tension (Sec. S2.3), a different constitutive model for arteries (Sec. S2.4), the role of raised intraocular pressure (Sec. S2.5) and explore the dynamics of the recovery phase in more detail (Sec. S2.6).

S2.1 Prescribed pressure boundary conditions

To examine how our results depend on the no-flux proximal and distal boundary conditions, in Fig. S2 we consider a prescribed pressure boundary condition for comparison (pressure set equal to the baseline pressure $p = 0$ at each end). This choice allows fluid to leave the system, so the compression in region 3 propagates from both ends (rather than just the junction between

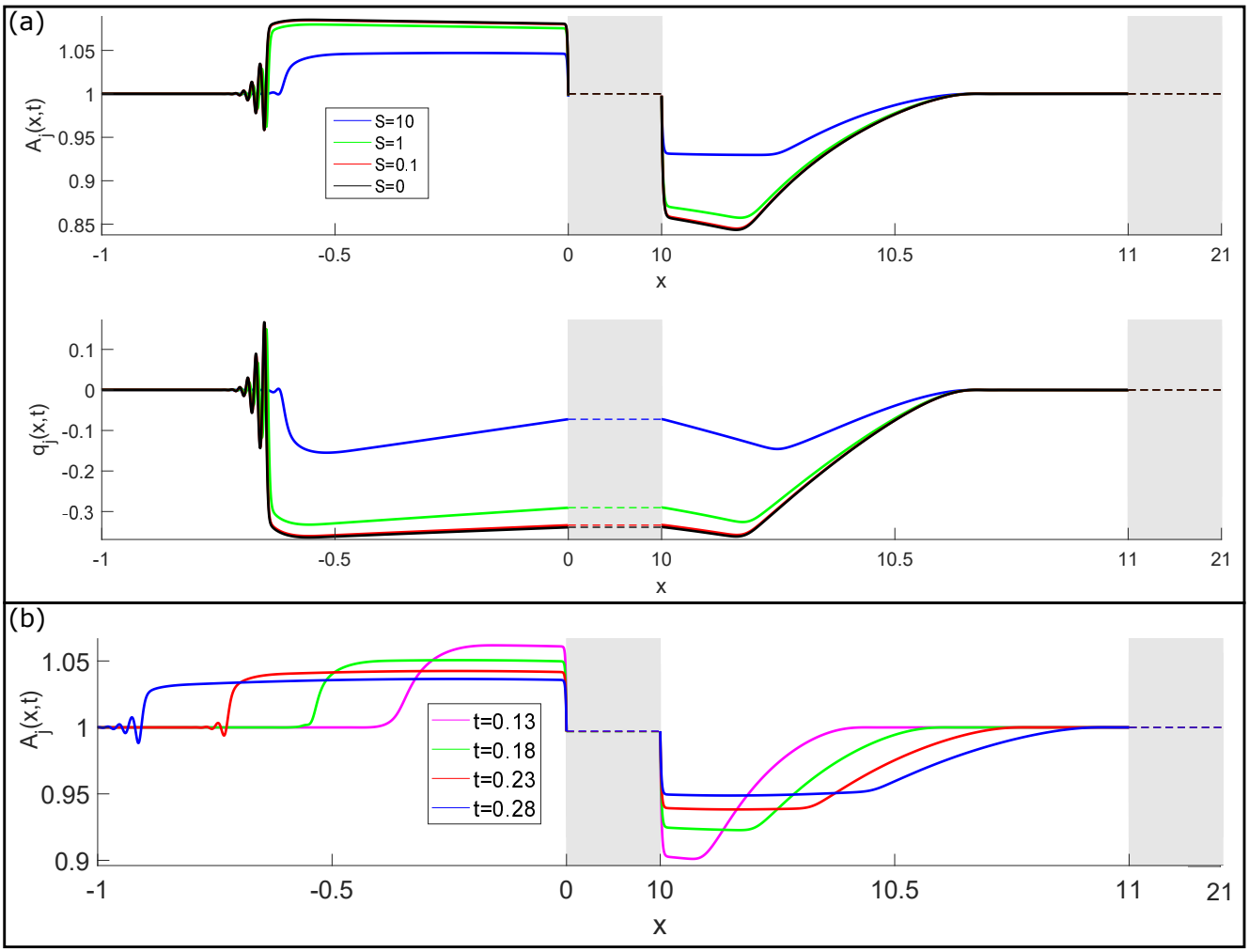

Figure S3: Response to an external forcing of $\Delta p = 75$ applied over $t_{ap} = 0.1$ in the presence of fluid viscosity: (a) spatial profile of cross-sectional area for four different values of the (dimensionless) viscosity parameter $S = 0$ (black line), $S = 0.1$ (red line), $S = 1$ (green line) and $S = 10$ (blue line). (b) Snapshots of the spatial profile of the vessel cross-sectional area for $S = 10$ at later times ($t = 0.13$: magenta, $t = 0.18$: green, $t = 0.23$: red, $t = 0.28$: blue).

regions 2 and 3). In particular we plot the spatial profile of the wave at a fixed instance in time, comparing the case with prescribed downstream pressure (red solid line) to the case with prescribed downstream flux (blue dotted line). Initially the choice has no effect on the expansion in region 1 (Fig. S2). However, at later times we expect differences after the upstream and downstream propagating wave-fronts in region 3 interact and reinforce the wave being transmitted in region 1.

S2.2 The influence of blood viscosity

For the baseline parameters of the central retinal vessels (see Tables 1 and 2 in the main text) we estimate the (dimensionless) viscous coefficient S (derived in Eq. (S28) above) as

$$S \approx 2.59207, \quad \text{(artery)}, \qquad S \approx 11.1111, \quad \text{(vein)}. \tag{S29}$$

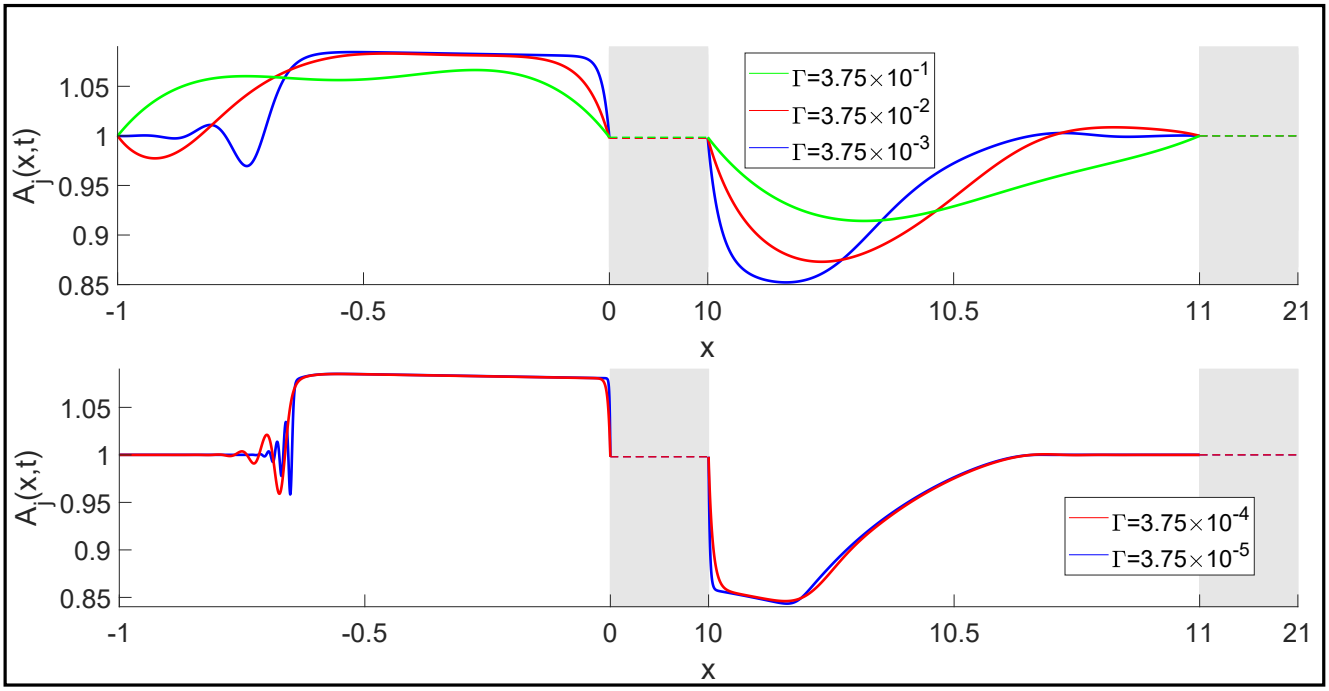

Figure S4: The influence of membrane tension on the response to a pressure perturbation of amplitude $\Delta p = 75$ applied over $t_{ap} = 0.1$, plotting the spatial profile of the vessel cross area at $t = 2t_{ap}$ for different values of the dimensionless tension parameter. In particular, the top panel shows larger values than those considered in the main paper, $\Gamma = 3.75 \times 10^{-1}$, $\Gamma = 3.75 \times 10^{-2}$ and $\Gamma = 3.75 \times 10^{-3}$ while the bottom panel shows values comparable to those considered in the main paper, $\Gamma = 3.75 \times 10^{-4}$ and $\Gamma = 3.75 \times 10^{-5}$.

To assess the role of blood viscosity in the dynamics presented in the main paper, in Fig. S3 we consider the behaviour for a baseline case with a pressure perturbation of $\Delta p = 75$ applied over a timescale of $t_{ap} = 0.1$ plotting spatial profiles of both the vessel cross-sectional area (Fig. S3a, top) and the axial flux (Fig. S3a, bottom) for different values of the viscosity parameter $S = 0$ (the inviscid limit considered in the main paper), $S = 0.1$, $S = 1$ and $S = 10$, all plotted at the same fixed time. For low values of S (≤ 1, where viscous effects are small) we observe very little difference between the profiles compared to the inviscid limit. For larger values of S (*eg.* $S = 10$ in Fig. S3a, where the effects of viscosity are strong) the overall shape of the cross-sectional area and flux profiles are still qualitatively similar to the inviscid case, although the amplitude of the pressure profile is reduced and the steep front has not fully formed by the time we plot the profile in Fig. S3(a). However, waiting slightly longer the sharp front will still eventually form (several snapshots shown in Fig. S3(b) at slightly later times). Hence, viscous effects reduced the amplitude of the pressure wave and slightly delay its formation. The cases shown here come close to spanning the operating range of the central retinal vessels, suggesting viscous effects do not strongly influence the mechanisms of pressure transmission reported in the main paper.

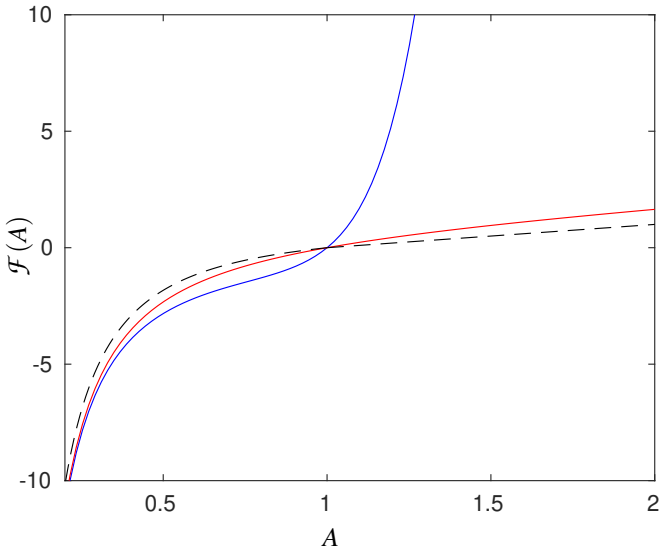

Figure S5: Different constitutive models for the vessel response to changes in transmural pressure, showing our choice of tube law from the main paper $\mathcal{F} = (A^{10} - A^{-3/2})$ (blue solid line), the revised tube law for arteries considered here $\mathcal{F} = (A - A^{-3/2})$ (red solid line) and the tube law considered by Cancelli & Pedley (1985) [2] (black dashed line).

S2.3 The role of membrane tension

To allow us to enforce continuity of cross-sectional area between regions we incorporate a membrane tension term into the model. This term raises the order of the spatial derivatives in the system by two, but introduces another dimensionless parameter (Γ) which has not been reliably measured *in vivo*. To assess the role of this membrane tension parameter, in Fig. S4 we examine the case of $\Delta p = 3000$ for $t_{ap} = 0.1$ for five different values of Γ spanning four orders of magnitude. When the membrane tension parameter is small (as for all the figures in the main text and Fig. S4 bottom panel), we observe a sharp change in the area profile along the tube length (surrounded by short wavelength dispersive waves on either side). Although the system is not formally multi-valued due to the tension of the wall, this sharp change in gradient occurs near the predicted location of the shock front from the shock capture code, and indicates a rapid expansion of the cross-sectional area over a short lengthscale. For larger values of the tension parameter (Fig. S4 top panel) the lengthscale of the pressure perturbation gradually expands across the entire of region 1, preventing the localised front reported in the main text (and seen in Fig. S4 bottom). Hence, for sufficiently large Γ (in this case $\Gamma \gtrsim 10^{-2}$) the propagating wavefront will eventually be suppressed by the influence of axial tension.

S2.4 The arterial tube law

In the main text we prescribe a functional form for our elastic 'tube law' in both the arteries and veins in the form of Eq. (2.6) depending on exponents m and n. In the main text we choose these exponents as $m = 10$ and $n = 3/2$, based on a model of the giraffe jugular vein (as opposed to an artery) [1]. This functional form is plotted in Fig. S5 as a blue line. The large exponent in expansion means that the tube rapidly stiffens as it expands, so the system must exert very large

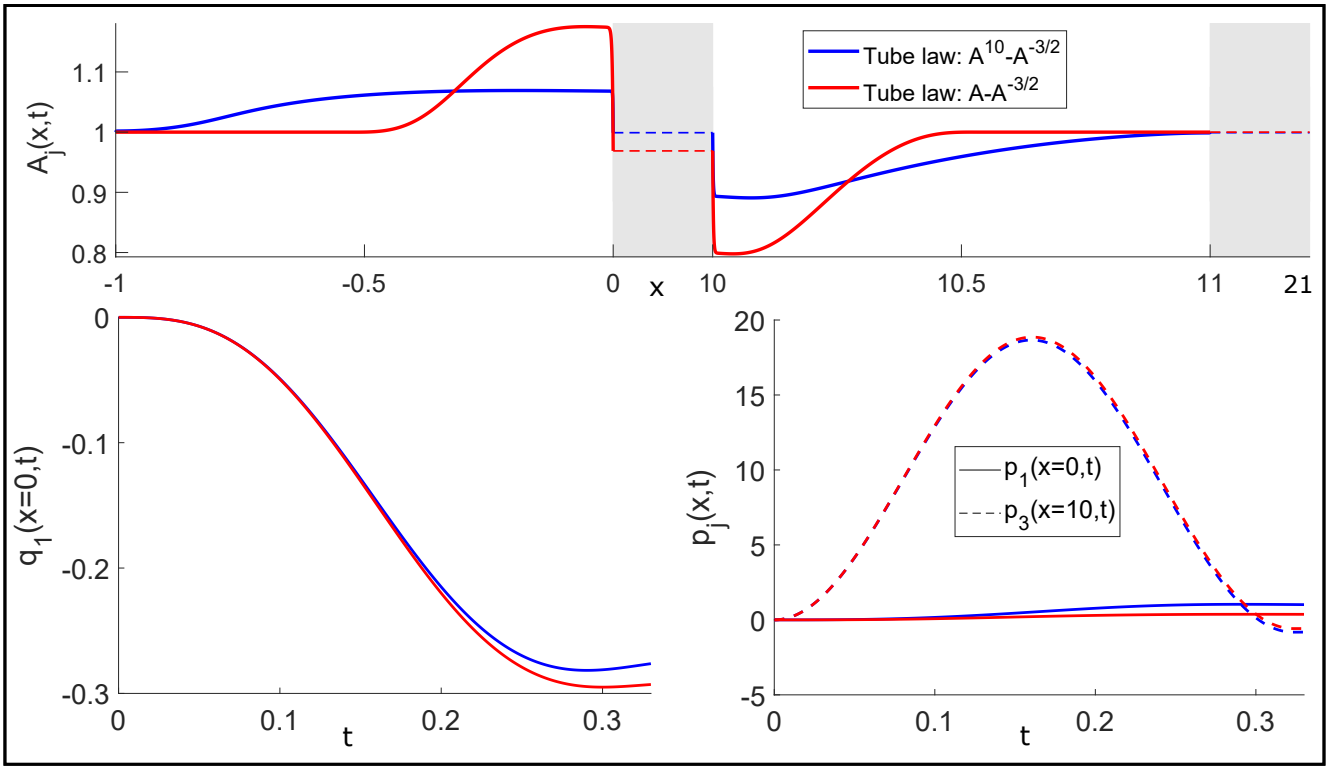

Figure S6: The response to an external pressure perturbation of $\Delta p = 19.1$ over a time interval of $t_{ap} = 0.323$ for two different choices of the arterial tube law, using $\mathcal{F} = A^{10} - A^{-3/2}$ (blue lines) and $\mathcal{F} = A - A^{-3/2}$ (red lines) showing: (top panel) the spatial profile of the vessel cross-sectional area at $t = 0.33$; (bottom left panel) temporal change in the axial flux at the junction between regions 1 and 2; (bottom right panel) temporal change in the pressure at the boundary between regions 1 and 2 (solid lines) and at the boundary between regions 2 and 3 (dashed lines).

pressures to see small changes in cross-sectional area. To better mimic the behaviour of an artery, in this subsection we use a modified choice of exponents based on the tube law used by Cancelli & Pedley [2] setting $m = 1$ and $n = 3/2$, plotted as the solid red line in Fig. S5; note that this choice is slightly different to their functional form, shown as a dashed line in Fig. S5, which has a discontinuous derivative at $A = 1$ and leads to some numerical difficulties in our approach.

In Fig. S6 we consider the behaviour of the full (four compartment) model with this modified 'tube law' using the membrane tension model with the parameter values for an artery and pressure perturbation $\Delta p^* = 380$ mmHg applied over $t^*_{ap} = 0.2$ ms (and using $\Gamma = 5.7 \times 10^{-6}$). In particular, in Fig. S6 top we plot the profile of the perturbation (solid red line), compared to a simulation with identical parameter values using the tube law of the main paper (solid blue line). We further compare the temporal profiles of the fluid flux through region 2 (Fig. S6 bottom left) and the pressure (Fig. S6 bottom right) at the junctions between region 1 and 2 (solid) and the junction between regions 2 and 3 (dashed). In our revised choice of arterial 'tube law' the artery is much more free to expand than before, hence the pressure disturbance drives a pressure wave of substantially larger amplitude in region 1, but progressing at a slower speed, compared to that with the tube law of the main paper. Such a response is to be expected since the linearised wavespeed of the system is substantially smaller with this tube law ($c_0 = \sqrt{5/2}$, compared to

$c_0 = \sqrt{23/2}$ with the original tube law). However, despite these quantitative differences the overall picture remains unchanged, with a similar mechanism of pressure transmission resulting in a pressure pulse rapidly propagating toward the eye in both cases.

S2.5 The role of raised intraocular pressure

The intraocular pressure (external to region 1 of our model) is typically larger than the intracranial pressure (external to region 3 of our model) by approximately 10 mmHg in a normal human eye. This difference can be even greater in patients with glaucoma or other eye diseases.

To assess the influence of this external pressure difference, in this subsection we consider a modified base state for our full four region model (described in Sec. 2(a-c) of the main paper) where the baseline pressure external to region 1, denoted p^*_{c0}, is elevated compared to region 3, denoted p^*_{e0}. In particular, we consider an arrangement where the baseline blood pressure in the vessel is constant and set equal to p^*_{c0} (*ie* $p^*_0 = p^*_{c0}$), which is greater than p^*_{e0} by an amount $\Delta p^*_c = p^*_{c0} - p^*_{e0}$. This assumption means that before the pressure perturbation is applied the tube remains of uniform area in region 1 (equal to its baseline value $A^*_1 = A^*_0$) and is inflated across region 3 to accommodate the transmural pressure. This arrangement is somewhat simplified (neglecting the possibility that the blood pressure along the vessel could be different to the external pressure in the baseline case), but allows us to examine the role of differential (baseline) external pressures within the confines of our model. In particular we illustrate an example using parameter values appropriate to the CRV with Δp^*_e=10 mmHg, where the corresponding inflated profile of the tube cross-sectional area across region 3 is shown in Fig. S7(a). Note that we use the numerical model with membrane tension (described in Sec. S1.2 above) to ensure that we can enforce continuity of cross-sectional area at both ends of the tube, but use a small value of the dimensionless membrane tension ($\Gamma = 5 \times 10^{-4}$) to ensure that the profile is uniform across most of the interior of region 3 with very narrow boundary layers (of width $\Gamma^{1/2}$) at the edges (to satisfy the continuity of area constraints), as shown in the inset to Fig. S7(a).

We apply a pressure perturbation external to region 3 of amplitude $\Delta p^* = 50$ mmHg over a time interval of $t^*_{ap} = 0.0005$ s (shown as dot-dashed line in Fig. S7) and measure the corresponding pressure in the intermediate rigid region (Fig. S7b), the change in cross-sectional area at the centre of region 1 (Fig. S7c) and the corresponding flux driven into region 1 over time (Fig. S7d). In all figures we compare to the corresponding case with $\Delta p^*_c = 0$ mmHg with all other parameters chosen the same, shown as a dashed line. These figures illustrate that the inflated profile across region 3 makes no qualitative and little quantitative difference to the pressure propagation behaviour across region 1, where in each case the system exhibits a pressure pulse moving at high speed toward the eye and the area profiles (Fig. S7b) and flux timetraces (Fig. S7d) are almost identical. It should be noted that the dynamics across region 3 are quite different between the cases (not shown), but it is interesting that this makes little difference to the behaviour in region 1.

S2.6 The recovery phase

Once the pressure perturbation has been fully applied the system will recover toward the baseline conditions as the induced pressure pulse moves into the eye away from the source and spreads through the retinal circulation. We examine this recovery by examining the response of the retinal vein with a short region 2 ($L_2 = 0.1$) to a pressure perturbation of amplitude $\Delta p^* = 0.75$ mmHg applied over $t^*_{ap} = 0.5$ ms. In particular we plot a typical profile of the tube cross-sectional area

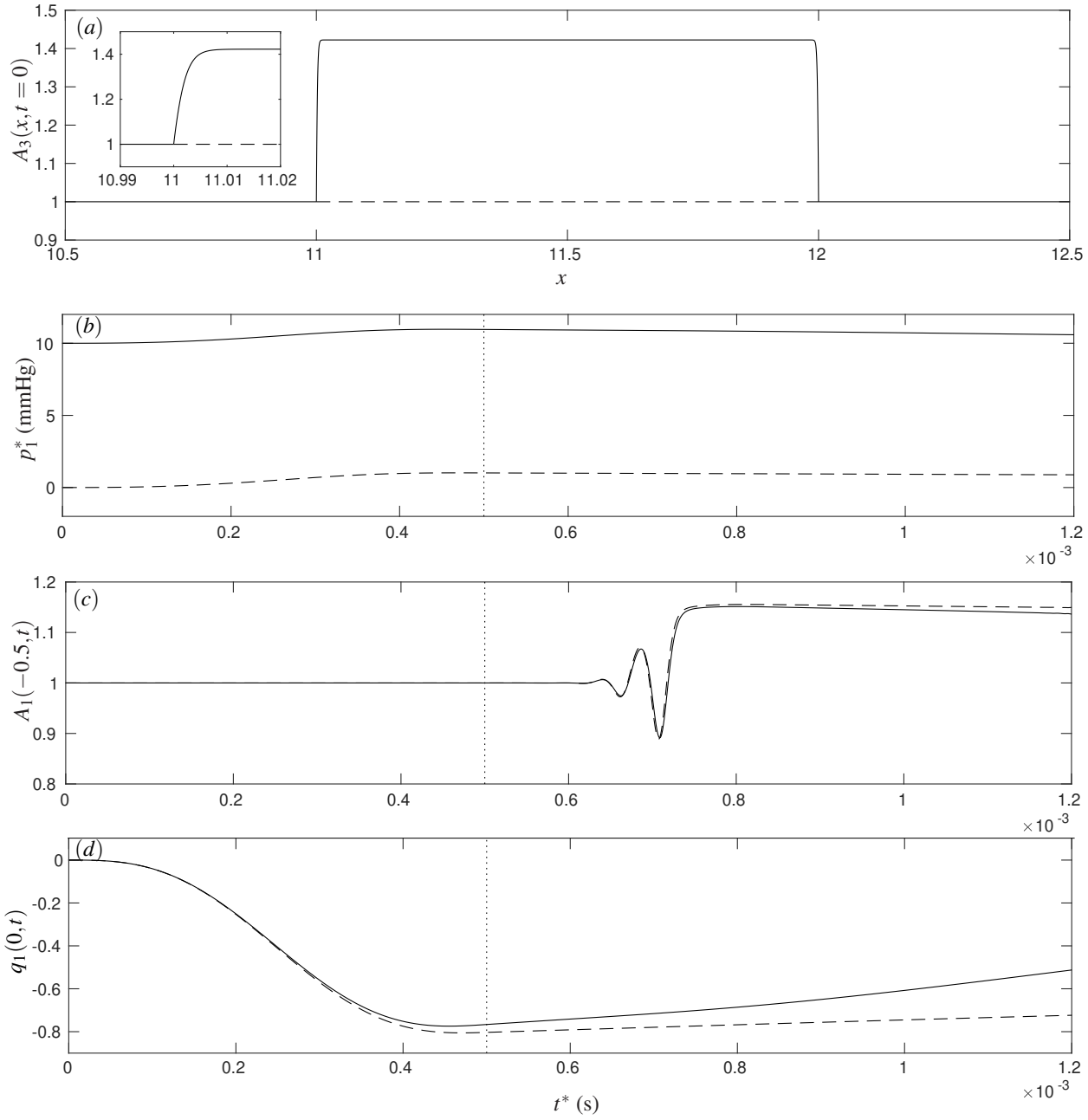

Figure S7: Response to a pressure perturbation of $\Delta p^* = 50$ mmHg over a time interval of $t^*_{ap} = 0.0005$ s with a external pressure difference of $\Delta p^*_c = 10$ mmHg (solid lines) using the membrane tension code with $\Gamma = 5 \times 10^{-4}$. We show: (a) the initial inflated spatial profile of the tube cross-sectional area across region 3; the time evolution (in dimensional variables) of (b) blood pressure at the junction between regions 1 and 2; (c) dimensionless vessel cross-sectional area at a fixed spatial location $x = -0.5$; (d) dimensionless axial flux at the junction between regions 1 and 2. In all panels we compare to simulation with $\Delta p^*_c = 0$mmHg (shown as dashed lines). The inset in panel (a) shows the narrow boundary layer in the tube profile at the junction between regions 2 and 3.

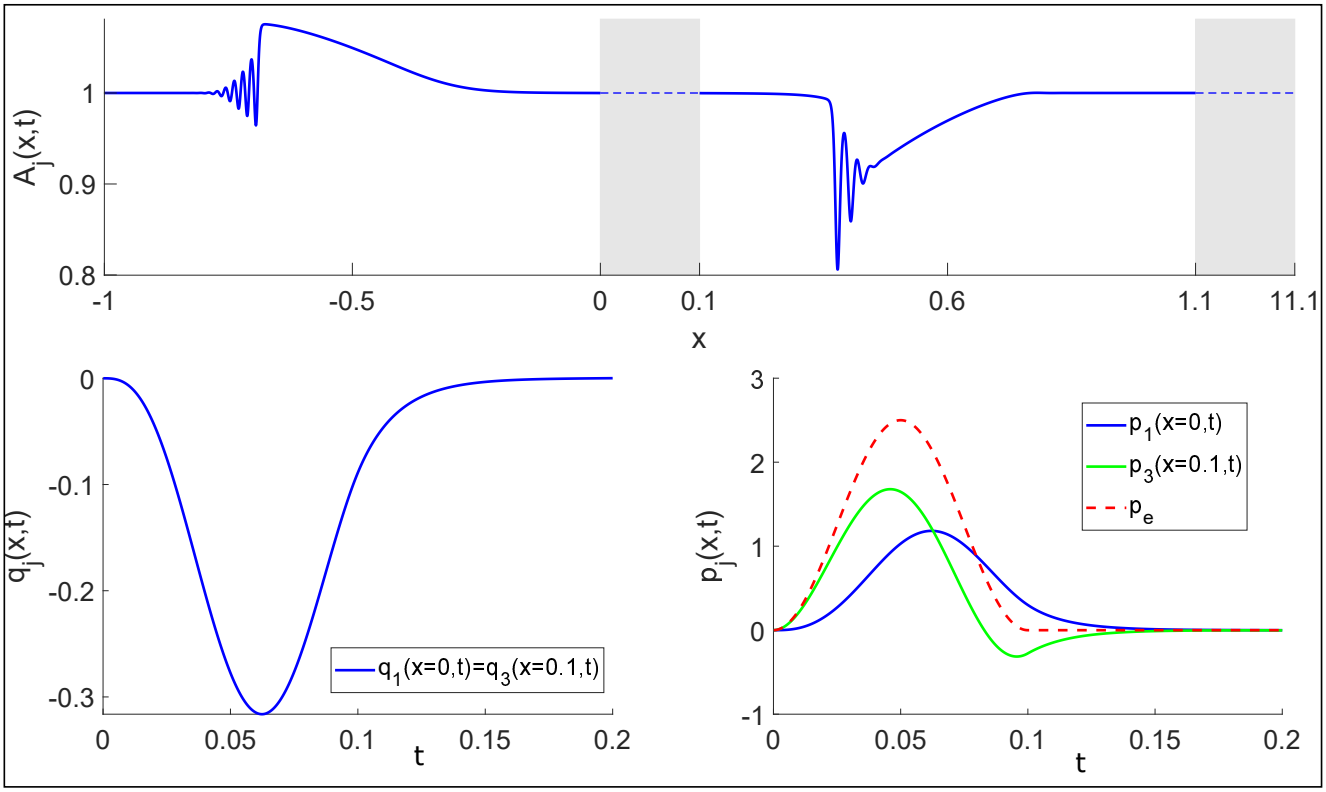

Figure S8: Recovery of the vessel profile back to equilibrium in response to pressure perturbation of amplitude $\Delta p = 2.5$ applied over $t_{ap} = 0.1$, and with $L_2 = 0.1$ (identical to Fig. 2(b) in the main text), showing: (top panel) spatial profile of the vessel cross-sectional area at time $t = 0.2$; (bottom left panel) temporal change in the axial flux at the junction between regions 1 and 2; (bottom right) temporal change in the fluid pressure at the junction between regions 1 and 2 (blue line), at the junction between regions 2 and 3 (green line) and the applied external pressure on region 3 (red dashed line).

(Fig. S8, top) and illustrate the time evolution of the flux between the compartments (Fig. S8, bottom left) and the pressures at the two ends of the intermediate region (Fig. S8, bottom right). In this case the spatial profile of the pressure perturbation generated in region 1 is much shorter than the overall length of the region (Fig. S8, top). Hence, the temporal profiles behind the advancing front return to their baseline values relatively quickly. In this example both the flux and pressure at the junction between regions 1 and 2 monotonically return to equilibrium by $t \approx 0.15 = \frac{3}{2}t_{ap}$. In both cases the temporal profiles of flux and pressure strongly resemble the functional form of the applied external pressure (albeit stretched over a longer timescale).

To explore the recovery phase for longer L_2 is a difficult task as we require region 1 to be sufficiently long to prevent interaction between the propagating pressure wave and the upstream boundary. We defer this investigation to future work.

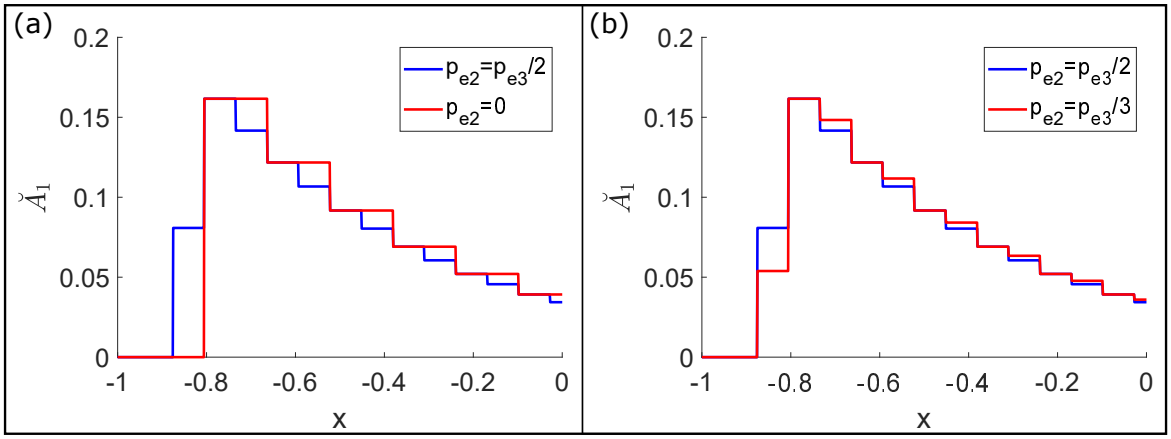

Figure S9: Spatial profiles of the vessel cross-sectional area in region 1 predicted using the analytical model in the case where an external pressure is applied to region 2 in addition to region 3. Profiles were obtained in response to a an external pressure $p_{e3} = 20$ in compartment 3 where $L_3 = L_1 = 1$ and $k_3 = k_2 = 1$ and an external pressure p_{e2} in region 2 of length $L_2 = 1$ and stiffness $k_2 = 200$: (a) spatial profiles of vessel cross-sectional area for $p_{e2} = \frac{1}{2}p_{e3}$ compared to $p_{e2} = 0$; (b) spatial profiles of vessel cross-sectional area for $p_{e2} = \frac{1}{2}p_{e3}$ compare to $p_{e2} = \frac{1}{3}p_{e3}$.

S3 Additional analytical results

In this section we modify our three region (linearised) analytical model to account for some proportion of the external pressurisation being applied to the intermediate (flexible) region 2 of the blood vessel (through the optic nerve) as well as region 3, mimicking compressive forces within the optic nerve itself.

S3.1 External pressure on the optic nerve sheath blood vessels

To consider these differential external pressures on the blood using the analytical model described in Sec. 2(d) of the main paper, we assume that there is an external pressure of magnitude p_{e2} (p_{e3}) applied to region 2 (region 3), applied for the same dimensionless perturbation time of $2L_2/\sqrt{k_2 c_0}$ as chosen in our analytical model. Following the same analysis as presented in the appendix to the main paper we obtain

$$\begin{aligned}
&\breve{A}_1(x+\sqrt{k_1c_0}t)) = \\
&\quad \begin{cases} \frac{2(p_{e3}-p_{e2})K_{12}}{(1+K_{32})(1+K_{12}))}\left[\frac{(1-K_{32})(1-K_{12})}{(1+K_{32})(1+K_{12})}\right]^n & K_{12}L_2(2n+1) < x+\sqrt{k_1c_0}t < K_{12}L_2(2n+3), n \geq 0 \\ 0 & \text{otherwise} \end{cases} \\
&+ \begin{cases} \frac{2p_{e2}K_{12}}{(1+K_{32})(1+K_{12}))}\left[\frac{(1-K_{32})(1-K_{12})}{(1+K_{32})(1+K_{12})}\right]^n & K_{12}L_2(2n) < x+\sqrt{k_1c_0}t < K_{12}L_2(2n+2), n \geq 0 \\ 0 & \text{otherwise} \end{cases}, \qquad \text{(S30)}
\end{aligned}$$

which we observe is equivalent to Eq. (A10) in the main paper when $p_{e2} = 0$ and $p_{e3} = p_e$ (with p_e defined in Eq. (A6) of the main paper). Note that all notation is identical to that used in the main paper. This final result is a summation of the effect we obtained from the external pressure

discontinuity between regions 2 and 3 added to the additional term arising from the external pressure discontinuity between regions 1 and 2. In this linearised system, applying a external pressures of p_{e2} to region 2 and p_{e3} to region 3 generates two waves in region 2, one originating at the junction between regions 1 and 2 (initially moving right) driven by a pressure difference p_{e2} and the other originating at the boundary between regions 2 and 3 (initially moving left) driven by pressure difference $p_{e3} - p_{e2}$. Due to linear superposition, the summation of these two waves has equivalent amplitude to that of a single wave of size $((p_{e3} - p_{e2}) + p_{e2}) = p_{e3}$. When these waves meet the boundary between region 1 and 2, energy is transmitted between the two regions and we see changes in the profile of region 1, exactly as in the previous models.

In Fig. S9 we illustrate two comparisons of this response using $k_2 = 200, k_1 = k_3 = 1, L_2 = 1$, showing the spatial profile of the pressure in region 1 at $t = 0.3$, taking $p_{e3} = 20$ in all cases and examining two particular comparisons, firstly with $p_{e2} = \frac{1}{2}p_{e3}$ compared to the the case with $p_{e2} = 0$ (Fig. S9a) and secondly with $p_{e2} = \frac{1}{3}p_{e3}$ compared to the case with $p_{e2} = \frac{1}{2}p_{e3}$ (Fig. S9b). We see that the spatial profile of the pressure wave in region 1 is essentially identical across all cases (albeit with slightly different discrete steps in each case) and has progressed a similar distance. Note that waves generated in cases with non-zero p_{e2} are slightly ahead because the initial pulse arrives in region 1 immediately rather than after the time taken for the wave to propagate from the boundary between regions 2 and 3.

In Fig. S9(a) we consider $p_{e2} = 0$, where there is just one wave generated in region 2 initially, and $p_{e2} = \frac{1}{2}p_{e3}$, with two initially generated waves of equal strength. The wavespeed in each region is constant throughout the simulation (due to linearity) and so when there is only one generated wave ($p_{e2} = 0$) the steps are exactly twice as long as those with non-zero p_{e2}. In the latter case every pair of steps indicates one full cycle of waves having propagated along region 2, been reflected by the junction and returned to their point of excitation (so the same total period). In Fig. S9(b) we see the the amplitude of p_{e2} influences the relative size of the jump at the start of each propagation-reflection cycle, but the total jump by the end of the cycle is the same.

Hence, from this model we can conclude that having an externally pressurised region 2 makes no qualitative difference to the predictions of the model. However, further work could evaluate how much effect non-linearities influence this result for larger amplitudes.

S4 Energy partition

In Sec. 3(d) in the main text, for sufficiently small k_2, we observe that when the pressure wave is propagating along region 2 and not interacting with either boundary there is an approximately equal partition between kinetic ($\mathcal{K}_2$) and stored elastic energy ($\mathcal{E}_2$). We justify this observation analytically in this subsection.

Similar to the derivation of the analytical model (Appendix A in the main text) we assume perturbations from the base state are small amplitude $\epsilon \ll 1$ and reduce to left and right moving waves within region 2, with flux and cross-sectional area profiles in the form

$$q_2 = \epsilon \left[f_2(x - \sqrt{k_2 v_0}t) + g_2(x + \sqrt{k_2 v_0}t) \right] + O(\epsilon^2), \tag{S31}$$

$$A_2 = 1 + \epsilon \frac{1}{\sqrt{k_2 v_0}} \left[f_2(x - \sqrt{k_2 v_0}t) - g_2(x + \sqrt{k_2 v_0}t) \right] + O(\epsilon^2). \tag{S32}$$

When the wave is not interacting with either boundary then one of f_2 or g_2 is identically zero (*ie* the wave is moving in one direction only) as our system is setup such that no additional waves can

be transmitted back into region 2 after they have left. Assuming $g_2 \equiv 0$, then from the definition of the energy budget (Eq. (2.10) in the main text) we can express $\mathcal{K}_2 = \mathcal{E}_2 + O(\epsilon^2)$ and so the kinetic energy and the stored elastic energy are equivalent at leading order. The argument is similar if $f_2 \equiv 0$.

References

[1] B. S. Brook, S. A. E. G. Falle and T. J. Pedley. Numerical solutions for unsteady gravity-driven flows in collapsible tubes: evolution and roll-wave instability of a steady state. *J. Fluid Mech.* **396**, 223–256, 1999.

[2] C. Cancelli and T. J. Pedley. A separated-flow model for collapsible-tube oscillations. *J. Fluid Mech.*, 157:375–404, 1985.

[3] T. J. Pedley. *The fluid mechanics of large blood vessels.* Cambridge University Press, 1980.

[4] P. S. Stewart, S. L. Waters, and O. E. Jensen. Local and global instabilities of flow in a flexible-walled channel. *Eur. J. Mech. B*, 28(4):541–557, 2009.

[5] P. L. Roe. Characteristic-based schemes for the Euler equations *Ann. Rev. Fluid Mech.*, 18(1):337–365, 1986.